JOURNAL OF SPACECRAFT AND ROCKETS
Vol. 44, No. 6, November–December 2007

Assessment of Experimental and Computational Transonic Base Pressure Using Flight Data

Makoto Ueno,* Yukimitsu Yamamoto,† and Masaaki Yanagihara‡
Japan Aerospace Exploration Agency,
Chofu, Tokyo 182-8522, Japan
Michel Leplat§
ONERA, F-92322 Châtillon, France
and
Jean Oswald¶
Centre National d'Etudes Spatiales,
91023 Evry, France

DOI: 10.2514/1.31144

The transonic base pressure distributions on a winged reentry vehicle configuration derived from wind-tunnel tests and computational fluid dynamics analyses are compared with flight data from the High Speed Flight Demonstration Phase II test. Results show that wind-tunnel forebody axial-force data agree well with the flight test data, but the base pressures differ. For a wind-tunnel model supported by a straight sting, base pressure correction using ventral model support data was found to be effective when the model was located far upstream of the roll pod. The base pressure obtained by computational fluid dynamics depends greatly on the number of grid points used in the base flow region, and it is shown that dense grids are able to reproduce the effect of the existence of the support sting despite the use of a classical turbulence model.

Nomenclature

CA	=	axial-force coefficient
CA_{ref}	=	arbitrary reference scale of the axial-force coefficient
CAF	=	forebody axial-force coefficient
CD	=	drag-force coefficient
Che	=	hinge-moment coefficient of the elevon
Chr	=	hinge-moment coefficient of the rudder
CN	=	normal-force coefficient
$CP\text{base}_{\text{ref}}$	=	arbitrary reference scale of pressure coefficient on the base, $CA_{\text{ref}} \cdot S/S_{\text{base}}$
D	=	reference diameter of the base, $\sqrt{S_{\text{base}}/\pi}$
M	=	Mach number
Re_{LB}	=	Reynolds number based on the body length
S	=	reference area
S_{base}	=	base area
α	=	angle of attack
β	=	sideslip angle
δe	=	elevator deflection angle (average of the left and right elevon deflection angles)
δr	=	rudder deflection angle (average of the left and right rudder deflection angles)

Presented as Paper 4566 at the 25th AIAA Applied Aerodynamics Conference, Miami, FL, 25–28 June 2007; received 21 March 2007; accepted for publication 19 July 2007.

*Researcher, Wind Tunnel Technology Center, Institute of Aerospace Technology. Senior Member AIAA.

†Senior Researcher, Computational Science Research Group, Institute of Aerospace Technology Center. Senior Member AIAA.

‡Manager, Flight Systems Technology Center, Institute of Aerospace Technology. Senior Member AIAA.

§Researcher, Applied Aerodynamics Department.

¶Engineer, Environment and Aerodynamics Department, Space Transportation Systems Directorate.

I. Introduction

REENTRY vehicles typically have a large base, and base drag forms a large component of subsonic drag for a reentry vehicle, sometimes accounting for almost half the total drag. Drag forces impact cross-range capability because engine thrust is not normally available during the return flight from orbit. Precise drag prediction techniques are therefore necessary for reentry vehicle development, and precise base pressure information is required to accurately determine aerodynamic characteristics. However, there are difficulties in predicting base pressure from wind-tunnel tests (WTT) and computational fluid dynamics (CFD); in wind-tunnel testing, interference effects from the model's support degrade the base pressure data, as summarized in [1], whereas with CFD, there are difficulties in computing separated flows.

The National Aerospace Laboratory and the National Space Development Agency carried out joint research on the H-II Orbiting Plane-Experimental (HOPE-X) unmanned experimental winged reentry vehicle [2–4] (Fig. 1), and these activities were taken over by the Japan Aerospace Exploration Agency (JAXA) when it was created from their merger. To help overcome the many technical difficulties in the development of such a system, a series of flight experiment programs [the Orbital Reentry Experiment (OREX) [5], the Hypersonic Flight Experiment (HYFLEX) [6], and the Automatic Landing Flight Experiment (ALFLEX) [7]] were completed and provided essential data [8]. A later flight experiment, the High Speed Flight Demonstration (HSFD), was conducted in two phases: phase I [9] in 2002 and phase II [10,11] in 2003. This paper presents the aerodynamic analysis of flight data from the HSFD phase-II (HSFD2) experiment.

HSFD2 was a drop test from a stratospheric balloon and was designed primarily to obtain the transonic aerodynamic characteristics of a reentry vehicle configuration to form a reference database for evaluating WTT and CFD data. A secondary objective was to establish design technology for a guidance and control system for the transonic flight of a reentry vehicle. The program was carried out collaboratively by Japan (JAXA) and France [Centre National d'Etudes Spatiales CNES)].

The HSFD2 flight test was conducted in July 2003 in Sweden [11]. Aerodynamic characteristics derived from flight test data were

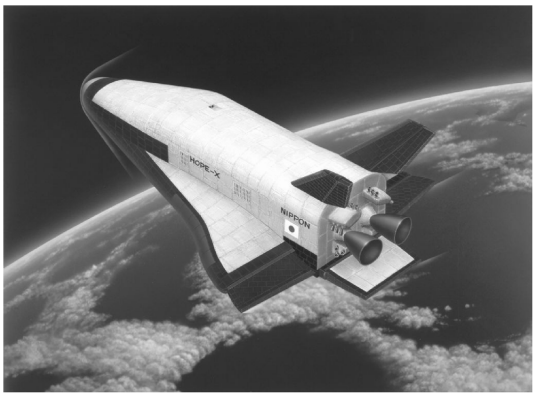

Fig. 1 Artist's impression of HOPE-X in flight.

compared with the results of wind-tunnel tests carried out by Japan and France [12–16] before and after the flight test. CFD analyses were also performed before [14] and after the flight test [15–18]. Cross comparisons between the flight data, the WTT, and the CFD analyses were performed. This paper presents the results of these comparisons regarding base pressure.

II. Flight Test

A. Flight Test Vehicle (Demonstrator)

The flight test vehicle (demonstrator) was a 25%-scale version of the 11HOPE configuration, the 1999 design iteration of the HOPE-X reentry vehicle. A three-view diagram of the demonstrator is shown in Fig. 2. Although the shape of the vehicle was designed to be as close to 11HOPE as possible, there were some differences, such as an air data sensor (ADS) probe attached to the nose, antennas mounted on the surface for communications, and the deletion of orbital maneuvering system (OMS) nozzles from the base. The demonstrator was controlled by dual rudders and elevons. Speed brakes attached behind the rudders were fixed at 40-deg deflection, and the body flap angle was set upward at 10 deg for trimming.

B. Measurement Parameters

The parameters to be measured relating to aerodynamic characteristics are listed in Table 1. All measurement instruments were prepared by JAXA, except for the body surface pressure sensors, which were prepared by CNES.

Air data were measured by an ADS mounted on the top of a nose boom. The ADS was based on a five-hole probe augmented by additional static pressure holes. Mach number, angle of attack, sideslip angle, static pressure, and dynamic pressure were computed from quantities measured by the ADS. To determine the pressure distribution over the vehicle, pressure measurements were made from the base, the body flap, and the body surface using pressure taps

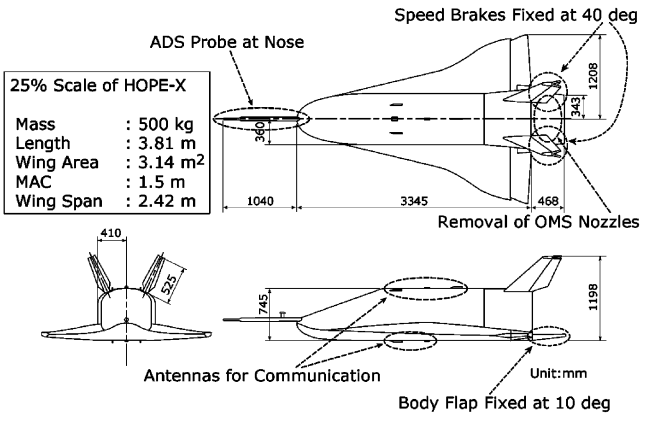

Fig. 2 Three-view diagram of the demonstrator.

Table 1 Measurement parameters related to aerodynamic characteristics

Category	Sensor	Parameters
Navigation data	HNU	Acceleration, angular velocity
Air data	ADS	Angle of attack, angle of sideslip, total pressure, static pressure, total temperature
Deflection angle	Potentiometer	Elevon, rudder
Hinge moment	Strain gauge	Elevon, rudder
Pressure distribution	Pressure sensor	Base (12 ports), body flap upper surface (4 ports), body surface (14 ports)

located as shown in Figs. 3 and 4. Components of acceleration and angular rate were measured by a GPS-augmented inertial navigation system called the hybrid navigation unit (HNU). Accelerations were multiplied by vehicle mass and nondimensionalized by dynamic pressure and the reference area to give aerodynamic coefficients. Elevon and rudder hinge moments were measured by hinge-moment balances installed in the control surface hinges. The definitions of the control surface deflection angles are shown in Fig. 5.

C. First Flight

In the nominal flight profile, the demonstrator is released from a stratospheric balloon at between 20–30-km altitude and accelerates in free fall to the Mach number designated for the test. The target Mach number is determined by selecting the release altitude range. Six flights at three Mach numbers (0.8, 1.05, or 1.2) were planned.

On reaching the target speed, the demonstrator initiates a constant-Mach flight phase, during which it maintains a Mach number and sideslip angle within specified tolerances while slowly reducing the angle of attack quasi statically. If the angle-of-attack rate is

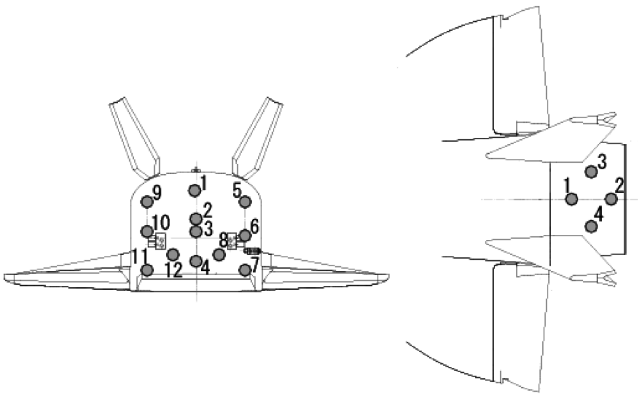

Fig. 3 Pressure ports on the base and the body flap.

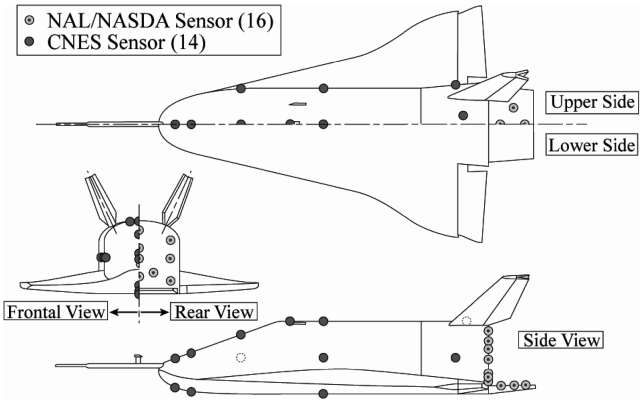

Fig. 4 Pressure ports on the body surface.

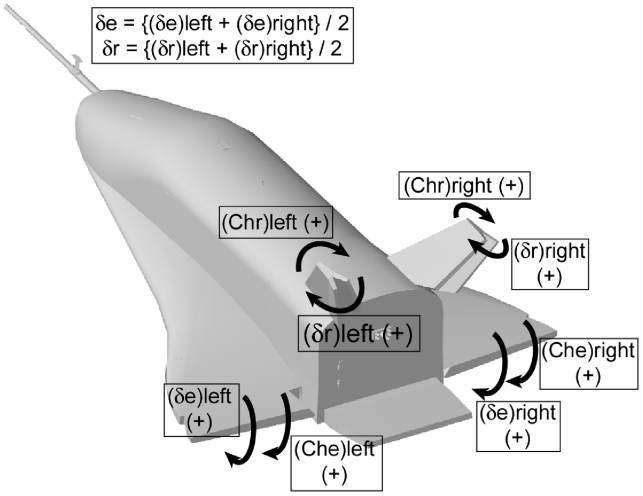

Fig. 5 Definition of control surface deflection angles and hinge moments.

sufficiently low, trimmed flight is maintained while the attitude changes, and longitudinal trimmed flight characteristics can be obtained over a wide angle-of-attack range. The data acquired during this phase form the bulk of data for postflight aerodynamic analysis. Following the constant-Mach phase, the demonstrator decelerates to Mach 0.75 and recovery guidance is initiated. The demonstrator autonomously selects a landing site from a number of candidate recovery areas and is guided to the site by flying around the surface of a virtual cylinder called the heading alignment cylinder. On reaching the site, the flight control computer issues commands to activate the recovery system, and the demonstrator touches down using air bags.

The first flight was performed on July 1, 2003 at the Esrange balloon site in Sweden. The target Mach number was set at 0.8. The demonstrator was released from an altitude of 21.3 km and carried out the constant-Mach-number data-acquisition flight phase. However, the recovery system did not work as expected and the demonstrator was damaged on touchdown, resulting in the cancellation of the remaining flights. The details of the first flight are described in [11].

Although recovery failed, the demonstrator completed the constant-Mach phase as required and aerodynamic measurements were performed successfully. The demonstrator was required to maintain Mach 0.8 $\pm$0.03 and a sideslip of 0 ± 2 deg while reducing its angle of attack from greater than 10 deg to less than 2.5 deg at a rate of less than 2 deg/s. The values of these parameters during the constant-Mach phase of the first flight are shown in Fig. 6 and meet the requirements.

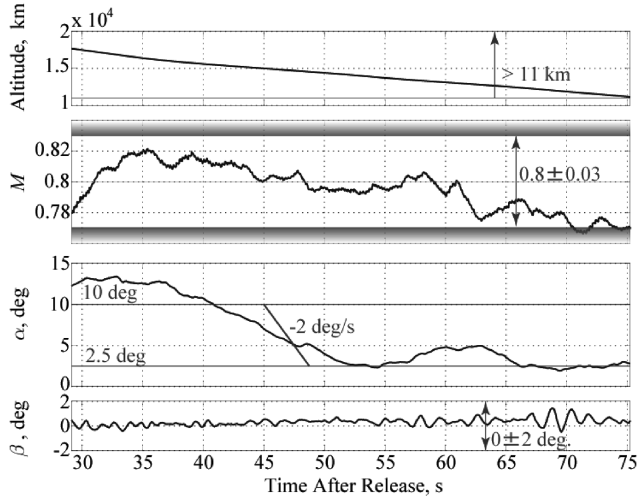

Fig. 6 Constant-Mach phase of the first flight.

III. Wind-Tunnel Test

Wind-tunnel tests on an HSFD2 model were performed both before and after the flight test. Because the aerodynamic design database used by the demonstrator's guidance and control software was derived from 11HOPE WTT data, the main objective of the preflight WTTs was to examine the effects of the differences between the 11HOPE and HSFD configurations, such as the ADS probe and antennas, and also to look at model support variations. Postflight WTTs were performed to acquire data for the same flight conditions as the flight test to enable precise comparison.

A. Wind-Tunnel Test Model

The HSFD2 wind-tunnel test model was an 18%-scale model of the demonstrator based on detailed CAD data and equipped with a mock ADS boom. The rudders were fixed at 0 deg and the elevons could be set at arbitrary angles. The speed brakes and body flap were fixed at the same angles as on the demonstrator.

Twelve pressure taps were installed on the base and four on the upper surface of the body flap in the same locations as on the demonstrator. Two taps corresponding to port numbers 2 and 3 on the base of the demonstrator (Fig. 3) were omitted because their locations coincided with the mounting hole for the sting support system. An additional 33 pressure taps were installed on the body and the surface of the right wing.

B. Postflight Wind-Tunnel Tests

Postflight wind-tunnel tests were carried out at the JAXA 2 m $\times$ 2 m Transonic Wind Tunnel and at the ONERA S2MA wind tunnel to obtain data under the flight test conditions for precise comparison with flight data. Data were obtained for elevon angles of 8, 9, and 10 deg, which were close to those used during the flight (Fig. 7), and at Mach numbers of 0.75, 0.8, and 0.85 to straddle the flight Mach number (Fig. 6). Because of the low air density at high altitude, the Reynolds number during the constant-Mach phase was sufficiently low to allow conventional wind tunnels to be used. The Reynolds number based on the body length (Re_{LB}) of the first flight and wind-tunnel tests ranged between 7×10^6 and 19×10^6, and values during wind-tunnel tests at Mach 0.8 were 8.9×10^6 at JAXA and 10.9×10^6 and 16.1×10^6 at ONERA. Roughness for boundary-layer transition was not required because the wind-tunnel Reynolds numbers were close to the flight Reynolds numbers.

1. *Wind-Tunnel Tests at JAXA*

The JAXA 2 m $\times$ 2 m Transonic Wind Tunnel (JTWT) was used for the Japanese wind-tunnel tests. This has a 2×2 m square-type test section with 20%-porosity walls perforated with normal holes. Total pressure can be controlled from 50 to 140 kPa, and the Mach number can be controlled from 0.1 to 1.4. Data were acquired in the "pitch-and-pause" mode.

Three campaigns were carried out at the JTWT: the first two in March 2004 and April 2005 and the third in June 2006 to examine the effect of sting interference on base pressure. In the first two campaigns, the HSFD2 model was supported by a conventional support sting, depicted in Fig. 8. In the last campaign, a sting with a longer tapered portion was used to avoid the influence of volumes downstream, such as the roll pod and the sting support strut. Length

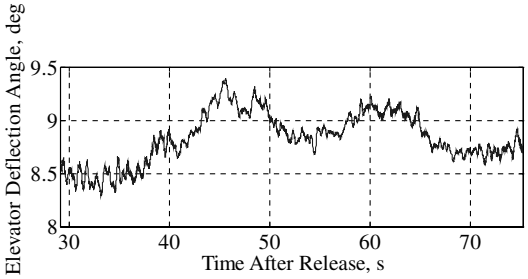

Fig. 7 Elevator deflection angle in flight.

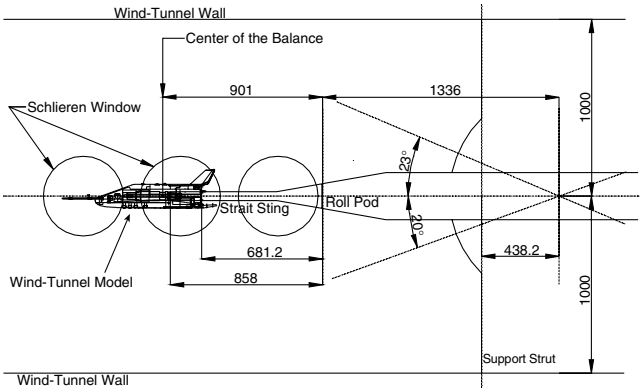

Fig. 8 Wind-tunnel model arrangement in the test section of the JTWT.

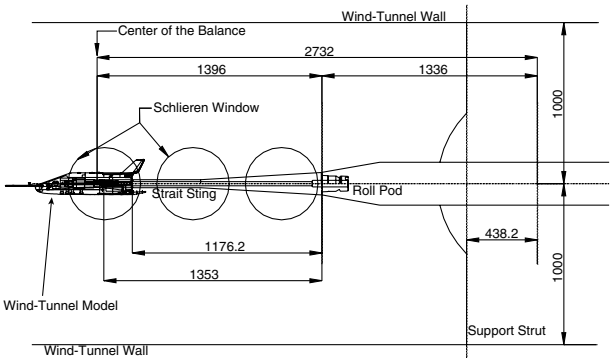

Fig. 9 Wind-tunnel model arrangement in the test section of the JTWT.

information for these stings is given in Table 2. The location of the model in the test section for the longer sting is shown in Fig. 9. In this paper, data from the last two campaigns are used for analysis.

The accuracies of the drag coefficient at Mach 0.8 and Reynolds number of 8.9×10^6 is 0.0012.

2. Wind-Tunnel Test at ONERA

The French WTT was performed at the ONERA S2MA wind tunnel, a closed-circuit continuous-flow transonic/supersonic wind tunnel that has a rectangular (1.77×1.75 m) test section in the transonic nozzle with perforated bottom and top walls with 2.9% porosity and 30-deg inclined holes. Total pressure can be controlled from 20 to 250 kPa, and the Mach number can be controlled from 0.1 to 1.3. The HSFD2 wind-tunnel test model was supported by a cranked sting with an 18-deg offset angle. Data were acquired during continuous angle-of-attack sweeps. Because of the sting offset, one polar was established by averaging the data at the normal position and the inverted position. The campaign was carried out in November 2004. Figure 10 shows the wind-tunnel test model in the test section.

The accuracies of the drag coefficient at Mach 0.8 and Reynolds number of 10.9×10^6 is 0.001.

3. Data Reduction

The test conditions for each wind tunnel are given in Table 3. To enable direct comparison with flight test results, linear models were built from each set of wind-tunnel test data. Reynolds number effect was examined in the ONERA S2MA by applying two levels of total pressure at Mach 0.8, and the effect was inserted into the models.

C. Comparison with Flight Test Data

To compare flight test results with WTT data, the flight test data were aligned at a frequency of 80 Hz and moving-averaged with a length of 101. The standard deviations of the removed oscillatory portions were calculated and scaled with the inverse of Student's T cumulative distribution function at 99% probabilities. These were considered as random errors in the data and were combined with systematic uncertainties to obtain the total uncertainties. Then, the moving averaged data and the uncertainties were decimated with an interval of 101 points. The systematic uncertainties were computed considering uncertainties of air data, HNU data, center of gravity location, mass properties, surface pressure, and manufacturing error of the demonstrator body surface. The total uncertainties in the flight test data are indicated in the following figures by error bars.

Table 2 Sting length

Sting	Distance between a roll pod and a model base	Length of straight part
JAXA conventional sting	681.2 mm = 4.65D	423.2 mm = 2.89D
JAXA longer sting	1176.2 mm = 8.03D	423.2 mm = 2.89D

Discrepancies in the axial-force coefficient CA between the flight test and the wind-tunnel tests are shown in Fig. 11. The graph shows that the WTT CA values are less than that of the flight test results by an almost constant amount. An arrow in the figure indicates an arbitrary reference scale CA_{ref}, which is used throughout this paper for comparison.

Forebody axial-force coefficients (CAFs) were computed by subtracting the base pressure contribution from the CAs. As a result, the differences between the WTT data and the flight test were reduced (Fig. 12). This indicates that the WTT CAFs are reliable, especially for the ONERA WTT, and that base pressure is the main reason for the CA discrepancies.

The averaged base pressures of the WTTs are shown in Fig. 13. The base pressures of the WTTs appear to be greater than those of the flight test, with a moderate angle-of-attack dependency. The $CP\text{base}_{\text{ref}}$ in the figure is a reference scale value that is defined as $CP\text{base}_{\text{ref}} = CA_{\text{ref}} \cdot S/S_{\text{base}}$.

The JAXA base pressure is closer to the flight test data than is the ONERA data. However, the base pressure distribution from the JAXA WTT shows stronger asymmetry (Fig. 14), whereas the ONERA WTT data show good symmetry both for positions and sideslip angles, and CAF shows better agreement with the flight test.

The asymmetry was considered to be caused by the presence of volumes downstream such as the sting, roll pod, and/or sting strut. The ONERA support system differs from JAXA's in that the distance between the support strut and the model is larger than that of the JAXA support system (Figs. 8 and 10). Thus, such volumes were supposed to be the cause of the base pressure asymmetry.

To improve the average values and the symmetry of the base pressure distributions, a further wind-tunnel test was performed at JAXA using a longer sting. A schematic of the sting and the WTT model is shown in Fig. 9. The straight portion has the same length as that of the conventional sting, whereas the total length from the end of the roll pod is almost double. The maximum of the angle of attack was limited to 9 deg, in consideration of the strength of the sting. As the result of the WTT with the longer sting, asymmetry was reduced, as shown in Fig. 15. The CAF also agrees very well with the ONERA data and the flight test (Fig. 16). The averaged base pressure was also improved and is the best value among the WTTs, as shown in Fig. 17.

D. Preflight Wind-tunnel Test for Support Interference

Use of a longer sting to improve the accuracy of the base pressure measurement also allowed a ventral support base pressure correction method to be used. As part of the preflight wind-tunnel tests, a ventral support system was used to examine the interferences caused by the straight sting support system. Details of the preflight WTT are described in [12]. A schematic of the ventral support system is shown in Fig. 18.

The blade of the ventral support sting has a flat hexagonal section. This offsets the WTT model by 201.15 mm vertically to avoid the influence of the roll pod. The base plate was replaced with a plate without the straight sting mounting hole. A dummy sting simulating a straight support can also be inserted into the base of the WTT model. When the dummy sting is used, the base plate with the straight

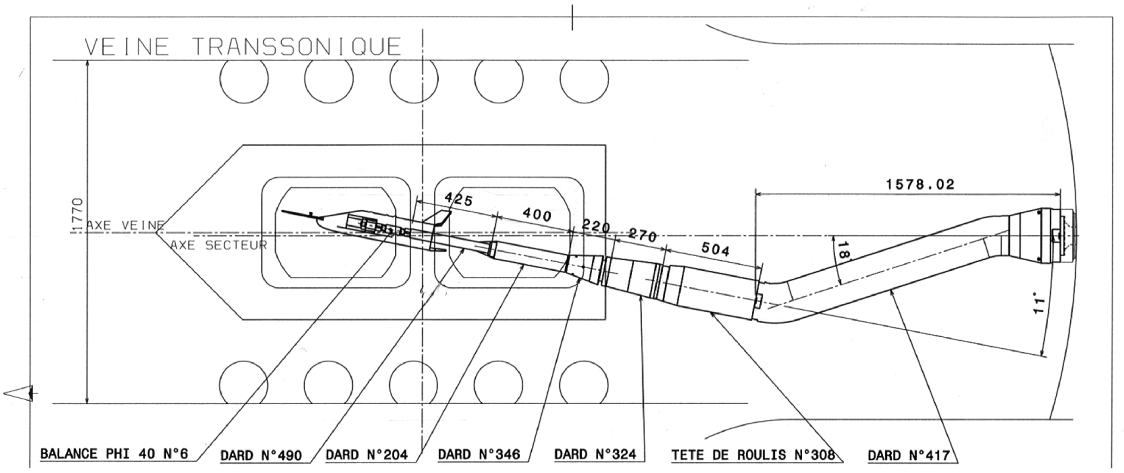

Fig. 10 Wind-tunnel model arrangement in the test section of the S2MA.

sting mounting hole is attached to the base and the hole is sealed with a cap, avoiding interference with the inserted dummy sting.

To examine the effect of the support system and the dummy sting on the base pressure, the preflight wind-tunnel test data were inserted into the linear model obtained from the postflight wind-tunnel test results. Although the postflight tests covered elevator angles of 8, 9, and 10 deg and Mach numbers 0.75, 0.8, and 0.85, the preflight wind-tunnel tests were performed at elevator angles of −20, 0, and 20 deg and Mach numbers 0.8, 1.05, and 1.2. Therefore, wind-tunnel data for a 0-deg elevator angle and Mach 0.8 were selected for comparison with the flight test data, and values for the 9-deg elevator angle point missing from the preflight data set were estimated using elevator effectiveness data from the postflight wind-tunnel tests.

Although the longer sting improved the base pressure measurements, discrepancy with the flight test results remained (Fig. 17). The modified base pressures from the ventral support tests are compared with the flight test and the longer straight sting WTT data in Fig. 19. It is remarkable that the base pressures obtained using the ventral support almost coincide with the flight test data. Additionally, the base pressure data obtained using the ventral support with a dummy sting show good agreement with the data obtained using the longer straight sting. This shows that the dummy sting can mimic the sting effect of the straight sting support if the straight sting is long enough to keep the wind-tunnel model away from downstream-volume elements.

IV. CFD

CFD analyses were also performed for the HSFD2. The computation conditions were selected to agree with those encountered in the flight test. The cases computed by JAXA are shown in Table 4 and those by ONERA are shown in Table 5. Angle of attack during the constant-Mach flight phase varied from approximately 14 to 2 deg, and two angle-of-attack points at approximately 4 and 8 were selected to be computed by both organizations, these being points at which the elevator deflection angle of the demonstrator in flight was 9 deg for the convenience of grid generation. In addition, case V at the angle of attack of 12 deg ($\delta e = 8.6$ deg) was selected to be computed only by JAXA. The CFD grids were developed based on detailed CAD model data.

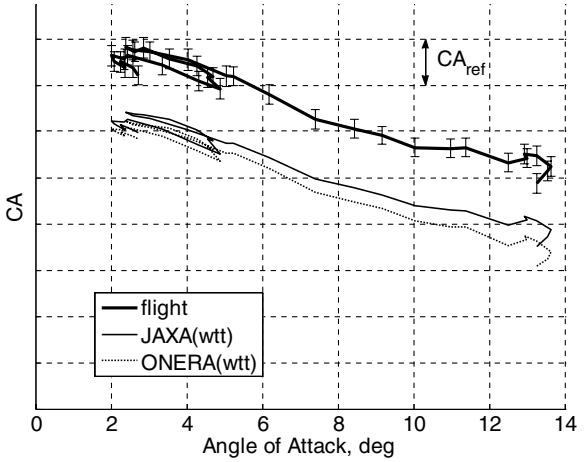

Fig. 11 Axial-force coefficient.

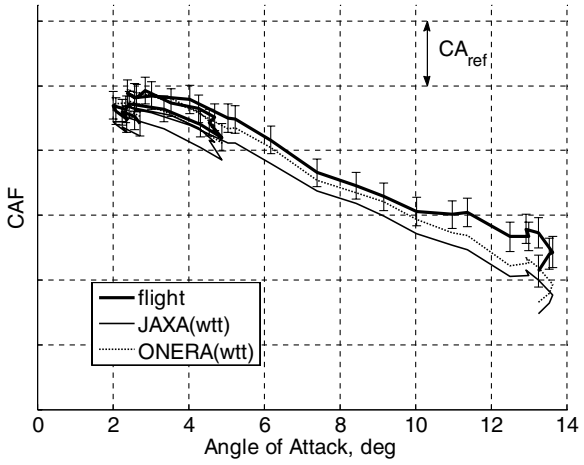

Fig. 12 Forebody axial-force coefficient.

Table 3 Wind-tunnel test conditions

	JAXA	JAXA (long sting)	ONERA
Mach number	0.75/0.8/0.85	0.75/0.8/0.85	0.75/0.8/0.85
Re_{LB} ($\times 10^6$)	8.6/8.9/9.1	8.6/8.9/9.1	10.1/10.9 and 16.1/11.6
α, deg	−5 to 20	−1 to 9	−5 to 20
β, deg	−5/0/5	−5/0/5	−5/0/5
δe, deg	8/9/10	8/9/10	8/9/10

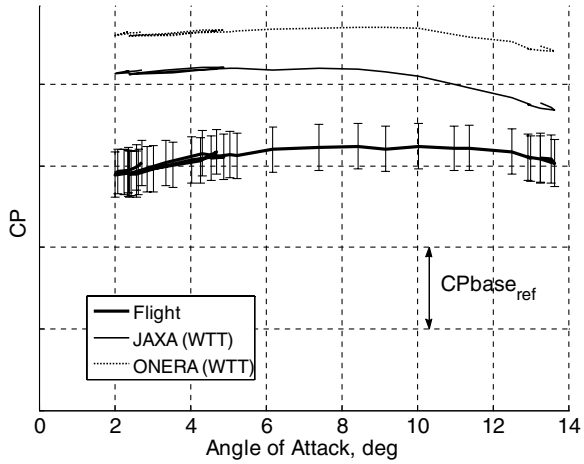

Fig. 13 Averaged base pressure coefficient.

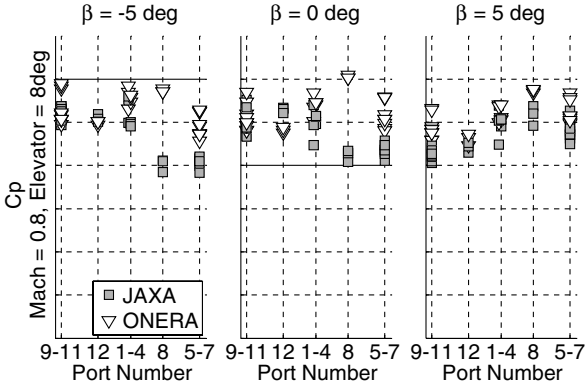

Fig. 14 Base pressure asymmetry.

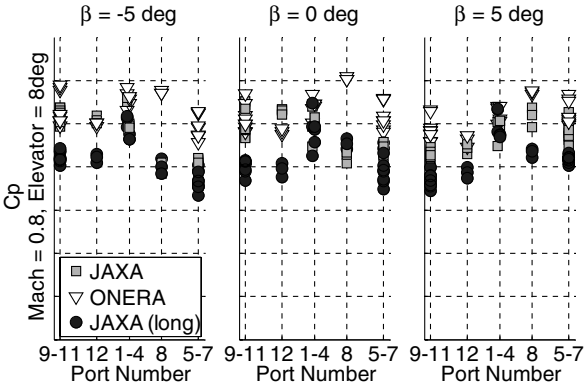

Fig. 15 Improvement of symmetry of base pressure distribution.

Regrettably, the flight test air data were further refined after the CFD conditions were selected, but by then the ONERA computation conditions could not be changed and so these differed from the flight conditions. However, the differences were slight and the conditions are considered to be practically the same.

CFD computations simulated the flight case and the WTT case: that is, free flight and with a support sting attached. The JAXA CFD WTT case represents the conventional support sting. The WTT case of each organization represents the sting used in their respective wind-tunnel tests.

A. JAXA CFD

A multiblock grid topology was used and there were about 8.5 million grid points. The grid did not model the small antennas on the body surface, the total temperature probe which stems from the ADS probe, and the open space behind the opened speed brakes.

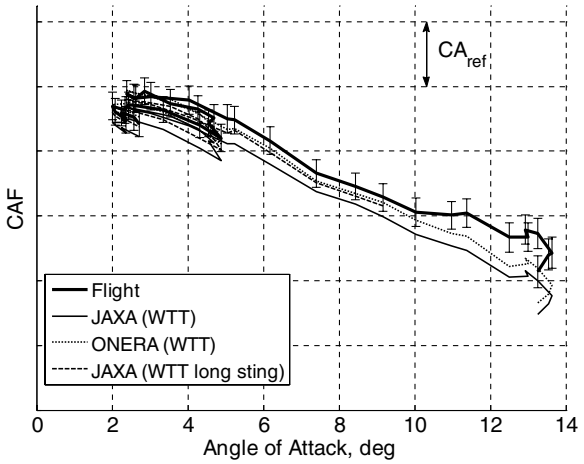

Fig. 16 Forebody axial-force coefficient.

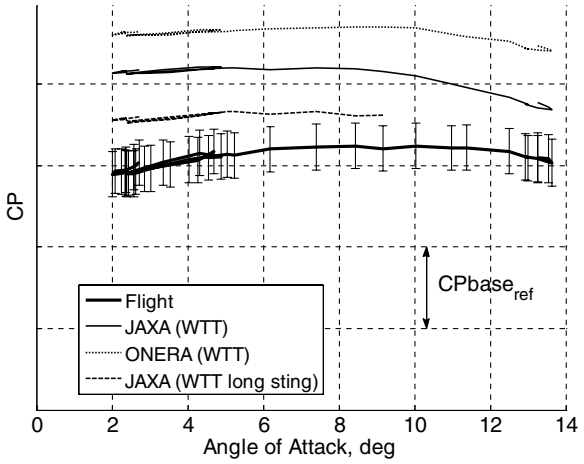

Fig. 17 Averaged base pressure coefficient.

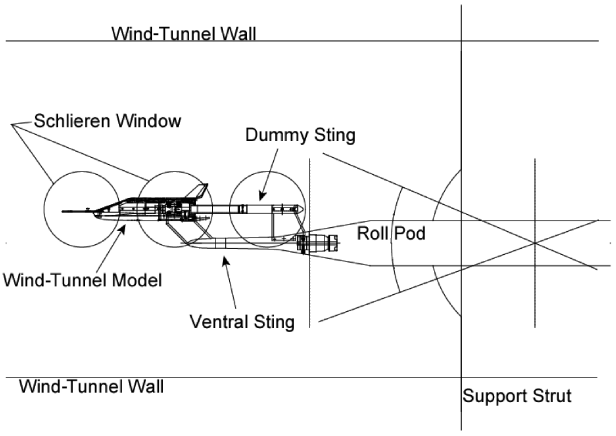

Fig. 18 Ventral support in the test section of the JTWT.

The JAXA computations were performed using in-house-developed software. A finite volume solver was used to solve Navier–Stokes equations, and Chakravarthy's total-variation-diminishing scheme was employed in the discretizations of the convective terms. An implicit approximate factorization method was used for time integration. The turbulence model was the Baldwin–Lomax model.

B. ONERA CFD

An O-type multiblock grid topology was used, and there were about 8 million grid points for 100 blocks. The 3D grid extended 10

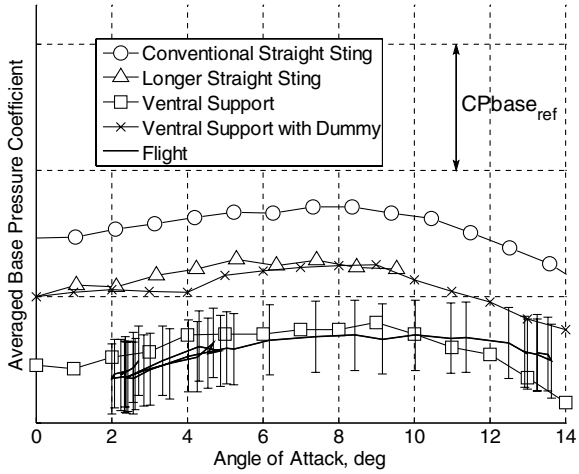

Fig. 19 Base pressure with the ventral support.

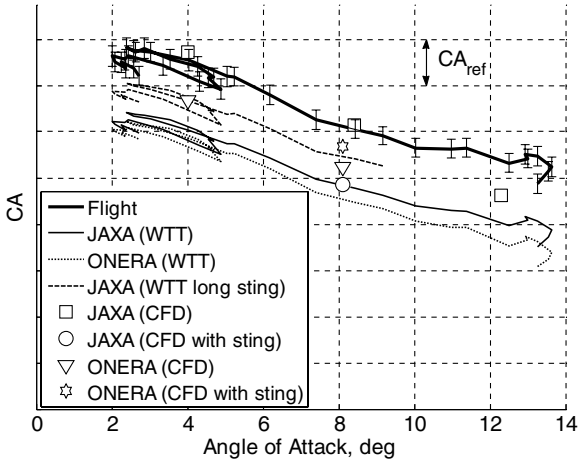

Fig. 20 Axial-force coefficient.

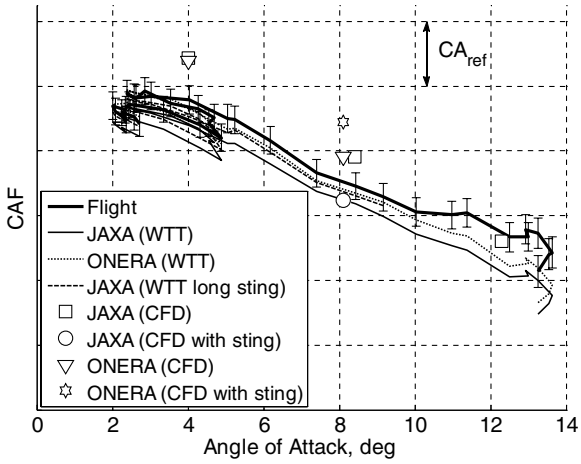

Fig. 21 Forebody axial-force coefficient.

times the body length in the upstream, downstream, and lateral directions. The geometry of the demonstrator was accurately modeled, including the ADS probe, all antennas, and the rudder speed brake. The effect of omitting the antennas from the CFD model was analyzed by the ONERA computation and was found to be less than 10% of CA_{ref}.

The computations were performed using ONERA's elsA software [18]. This is a cell-centered finite volume code solving the three-dimensional Reynolds-averaged Navier–Stokes equations on multiblock structured grids. The Navier-Stokes equations and turbulence transport equations were solved separately. For this study, the Jameson scheme was used, associated with the lower–upper symmetric successive over-relaxation implicit method for time integration, and Spalart–Allmaras turbulence model was employed.

C. Comparison with Flight Test Results

The axial-force coefficients *CA* of the CFD data are compared with the flight test data in Fig. 20. The JAXA CFD data agree well with the flight test data, and the data for the conventional sting case show the same order of difference as that between the flight and WTT data. The ONERA CFD data values are lower than those of the corresponding flight test data points but are rather close to the WTT data. The ONERA computations for the WTT case do not show the effect of the sting.

However, for the *CAF*, the CFD values excluding the WTT case of the JAXA data are greater than the flight values (Fig. 21), whereas the WTT *CAF* data agree well with the flight test data. This implies that the contribution of base pressure to the total *CA* in the CFD result is less than in the flight test, and the *CA* data from the JAXA CFD results do not agree closely enough. Thus, the CFD derived base pressures are comparatively greater than the flight test values.

The averaged base pressures of the WTTs are shown in Fig. 22. As stated earlier, the CFD base pressures are greater than the flight test values. The JAXA CFD data are closest to the flight test data, and the JAXA CFD data for the sting case yielded data very close to the conventional sting WTT. In the ONERA computation, presence of the sting induces a strong modification of the pressure distribution with a less homogeneous pressure field, but after integration, the averaged base pressure coefficient for the sting case results in very close to the CFD data for the flight.

Although none of the CFD base pressures were low enough to agree with the flight data, the JAXA CFD was able to show the differences between the free-flight and WTT conditions.

Table 4 JAXA CFD conditions

	Case II	Case III	Case IV	Case V
Flight/WTT	Flight	WTT	Flight	Flight
Mach number	0.80	0.81	0.81	0.81
Re_{LB} ($\times 10^6$)	11.7	11.0	10.6	9.33
α, deg	4	8.1	8.4	12.3
β, deg	0	0	0	0
δe (CFD), deg	9	9	9	8.6
δe (flight), deg	9	9	9	8.6

Table 5 ONERA CFD conditions

	Case II	Case III	Case IV
Flight/WTT	Flight	WTT	Flight
Mach number	0.80	0.81	0.81
Re_{LB} ($\times 10^6$)	11.7	11.0	10.0
α, deg	4	8.1	8.1
β, deg	0	0	0
δe (CFD), deg	9	9	9
δe (flight), deg	9	9	9

D. Discussion on CFD Results

Convergence of the computations was examined by looking not only at the evolution of the residuals, but also at the overall forces. For the ONERA computations, 5000–7000 iterations were sufficient to achieve convergence of the main coefficients (*CA* and *CN*) [16], and the *CA* residual was within 10% of CA_{ref}. On the other hand, the JAXA computation took a very long time to settle, such that the *CD* residual as large as 50% of CA_{ref} remained after more than 100,000 iterations. This longer settling time was considered to be due to the fact that local time stepping was not used. The reason for the larger residual is examined in the following discussion.

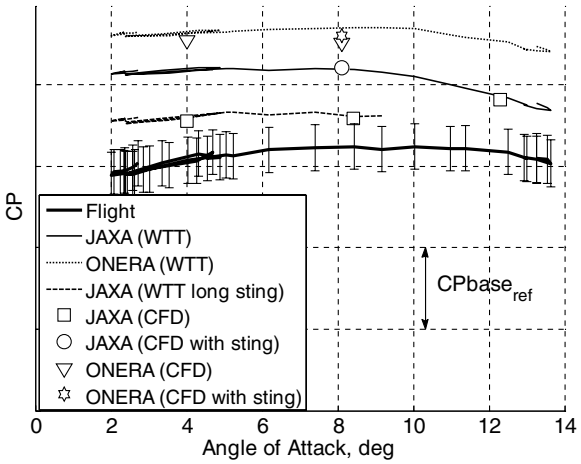

Fig. 22 Averaged base pressure coefficient.

a) Case III of ONERA

b) Case IV of ONERA

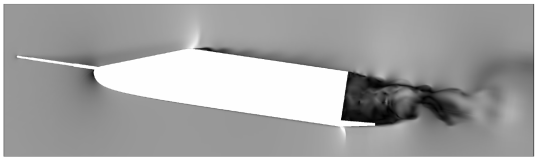

c) Case III of JAXA

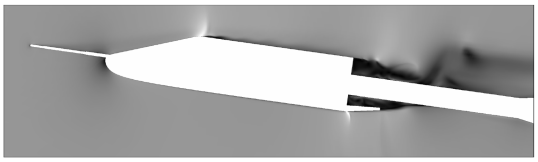

d) Case IV of JAXA

Fig. 23 Mach number contours of CFD.

The Mach number contours of cases III and IV at the symmetry plane of the demonstrator are shown in Fig. 23. All the CFD computations were able to show the flow separation behind the base of the demonstrator, whereas the JAXA computations showed the base flow vortices at finer resolutions and captured vortices being shed behind the base. This unsteady vortex shedding is considered to be the cause of large residuals in the JAXA computation.

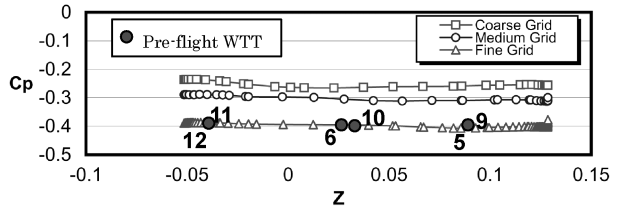

Fig. 25 Grid density influence on base pressure computation [17] (preflight WTT $M = 1.05$ and $\alpha = 0$ deg).

In a former study by JAXA [17], a higher grid density in the base flow area was shown to be effective in improving base pressure computation. In that study, three levels of grid density (Fig. 24) were examined, and it was found that using the finest grid, computations for the support-sting case gave base pressures very close to the preflight wind-tunnel test at a Mach number of 1.05 (Fig. 25). The postflight CFD analysis carried out by JAXA in the present paper employed still finer (121×241) grid points in the area than those in the former study, whereas ONERA used a grid of 37×71 points. The JAXA computation was thus able to capture detailed vortices (Fig. 23). It appears that the JAXA computation could resolve finer base flow structure than could the ONERA computation, and this brought about the lower base pressure values and enabled it to distinguish the existence of the support sting. Although neither the JAXA nor the ONERA CFD results gave base pressures as low as the flight test data, JAXA's grid density study showed that the small vortices of the base flow must be resolved to obtain adequately low base pressure. In such cases, local time stepping is inappropriate for base flow computation because the base flow is substantially unsteady and detailed vortices shed from the base region have to be captured.

V. Conclusions

The High Speed Flight Demonstration Phase II (HSFD2), a transonic free-flight drop test of a reentry vehicle model, was performed collaboratively by Japan [Japan Aerospace Exploration Agency (JAXA)] and France [Centre National d'Etudes Spatiales CNES)], and base pressure data from the flight test, wind-tunnel tests, and CFD were compared with each other.

The WTT data showed that use of a short straight support sting could cause asymmetry in the measured base pressure distribution. When a sting sufficiently long to avoid the influence of volumes downstream, such as the roll pod and the sting support strut was used, the base pressure asymmetry reduced and the forebody axial forces (CAF) measured in both the JTWT and the S2MA agreed well with flight test data. Use of a ventral support sting yielded measurements close to the flight base pressure data and enabled correction of the straight sting data by subtracting the effect of a dummy sting, provided that the straight sting was sufficiently long to avoid downstream-volume influence on base pressure. However, base pressure measurements differed between the wind tunnels, which implies that wind-tunnel users should examine the amount of correction using a dummy sting for each wind tunnel and support system.

CFD analysis using a high-density grid in the base flow region was able to distinguish the presence of the support sting despite the use of a classical turbulence model. However, base pressures as low as the flight test values could not be obtained.

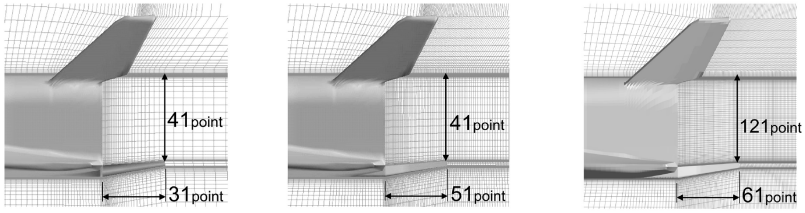

a) Coarse grid **b) Medium grid** **c) Fine grid**

Fig. 24 Grid density.

References

[1] Tuttle, M. H., and Gloss, B. B., "Support Interference of Wind Tunnel Models—A Selective Annotate Bibliography," NASA TM-81909, Mar. 1981.

[2] Tsujimoto, T., and Kouchiyama, J., "Current Status of the H-II Orbiting Plane-Experimental (HOPE-X) Development," International Symposium on Space Technology and Science, Paper 2000-g-06, May 2000.

[3] Ishimoto, S., Shirouzu, M., and Kouchiyama, J., "Modification of HOPE-X Aerodynamics Configuration," International Symposium on Space Technology and Science, Paper 2000-e-42, June 2000.

[4] Yamamoto, Y., and Kurotaki, T., "Numerical Aerodynamics Design Study of HOPE-11 Model at Supersonic/Hypersonic Flight Range," International Symposium on Space Technology and Science, Paper 2000-e-43, June 2000.

[5] Akimoto, T., Ito, T., Yamamoto, M., Bando, T., and Inoue, Y., "Orbital Re-Entry Experiment (OREX)—First Step of Space Return Flight Demonstrations in Japan," International Astronautical Congress Paper IAF-94-V.2.525, 9–14 Oct. 1994.

[6] Shirouzu, M., and Yamamoto, M., "Overview of the HYFLEX Project," AIAA Paper 96-4524, Nov. 1996.

[7] Nakayasu, H., and Nagayasu, M., "On the Automatic Landing FLight EXperiment (ALFLEX)," *Proceedings of the ALFLEX Symposium*, NAL SP-39T, National Aerospace Lab. of Japan, Chofu-shi, Tokyo, Aug. 1998, pp. 7–16.

[8] Shirouzu, M., Inouye, Y., Watanabe, S., Shigemi, M., Ueno, M., Yamamoto, Y., and Ito, T., "Overview of Aero- and Aerothermodynamic Researches on HOPE-X and Related Activities in Japan," AIAA Paper 2004-2426, Jul. 2004.

[9] Sarae, W., Nishizawa, T., Sagisaka, M., Akimoto, T., Yanagihara, M., and Miyazawa, Y., "An Overview of the High Speed Flight Demonstration Project Phase I," *3rd International Symposium on Atmospheric Reentry Vehicles and Systems* [CD-ROM], French Association for Aeronautics and Astronautics, Toulouse, France, Mar. 2003, Paper 24-024-P.

[10] Yanagihara, M., Miyazawa, Y., Akimoto, T., Sagisaka, M., Venel, S., and Guedron, S., "Current Status of High Speed Flight Demonstration Project Phase II," *3rd International Symposium on Atmospheric Reentry Vehicles and Systems* [CD-ROM], French Association for Aeronautics and Astronautics, Toulouse, France, Mar. 2003, Paper 24-058-P.

[11] Yanagihara, M., Miyazawa, Y., Munenaga, T., Venel, S., Guedron, S., and Cretenet, J.-C., "Results of High Speed Flight Demonstration Phase II," International Astronautical Congress, Paper 04-V.6.03, 2004.

[12] Ueno, M., Yamamoto, Y., Koike, A., Yanagihara, M., and Miyazawa, Y., "Pre-Flight Wind Tunnel Test of High Speed Flight Demonstration Phase II," AIAA Paper 2002-3064, June 2002.

[13] Ueno, M., Sarae, W., Tsujimoto, T., Yanagihara, M., and Hirotani, T., "Aerodynamic Characteristics Estimation of the High Speed Flight Demonstrator Phase II Using Flight Test Data," AIAA Paper 2004-4943, Aug. 2004.

[14] Yamamoto, Y., Ueno, M., Yanagihara., Y., Miyazawa, Y., and Ito, R., "Pre-flight CFD analysis of High Speed Flight Demonstrator Phase II Vehicle and the Validation of HOPE-X Transonic Aerodynamics," AIAA Paper 2002-685, Jan. 2002.

[15] Champigny, P., Leplat, M., Thorigny, P., Oswald, J., and Ueno, M., "Numerical and Experimental Investigations of the HSFD Transonic Aerodynamics," *4th International Symposium on Atmospheric Reentry Vehicles and Systems* [CD-ROM], French Association for Aeronautics and Astronautics, Toulouse, France, Mar. 2005, Paper 32-137.

[16] Champigny, P., Leplat, M., Thorigny, P., Oswald, J., Ueno, M., and Yamamoto, Y., "Numerical and Experimental Investigations of the HSFD2 Transonic Aerodynamics," International Symposium on Space Technology and Science, Paper 2006-e-10, June 2006.

[17] Yamamoto, Y., Totsuka, A., Yoshida, M., Ueno, M., Kawato, H., Hokiyama, K., Ishiyama, T., and Hosaka, Y., "Progress of Transonic Flow Simulation in the Analysis of HSFD Phase II Flight Experiment and the Design Problems of the Lifting Body Re-Entry Vehicles," International Symposium on Space Technology and Science, Paper 2004-e-12, Oct. 2004.

[18] Gazaix, M., Jolles, A., and Lazareff, M., "The elsA Object-Oriented Computational Tool for Industrials Applications," International Symposium on Space Technology and Science, Paper 2002-1.10.3.1, Sept. 2002.

R. Cummings
Associate Editor